UC Irvine
UC Irvine Previously Published Works

Title
Nonplanar Bouligand Architectures for Enhanced Mechanical Performance in Cementitious Composites

Permalink
https://escholarship.org/uc/item/6vm1p358

Journal
Advanced Materials, 38(64)

ISSN
0935-9648

Authors
Wang, Y
Shyamsunder, L
Dasika, PS
et al.

Publication Date
2026-11-17

DOI
10.1002/adma.75205

Copyright Information
This work is made available under the terms of a Creative Commons Attribution-NonCommercial-NoDerivatives License, available at https://creativecommons.org/licenses/by-nc-nd/4.0/

Peer reviewed

eScholarship.org Powered by the California Digital Library
University of California

Advanced Materials

ADVANCED MATERIALS
www.advmat.de

RESEARCH ARTICLE OPEN ACCESS

Nonplanar Bouligand Architectures for Enhanced Mechanical Performance in Cementitious Composites

Yu Wang[1] | Loukham Shyamsunder[1,2] | Phani Saketh Dasika[1] | Andrew Nguyen[3] | David Kisailus[3,4] | Jan Olek[1] | Jeffrey P. Youngblood[5] | Pablo D. Zavattieri[1]

[1]Lyles School of Civil and Construction Engineering, Purdue University, West Lafayette, Indiana, USA | [2]Department of Civil and Environmental Engineering, Indian Institute of Technology Tirupati, Andhra Pradesh, India | [3]Advanced Manufacturing Program, School of Engineering, University of California, Irvine, California, USA | [4]Department of Materials Science and Engineering, University of California, Irvine, California, USA | [5]School of Materials Engineering, Purdue University, West Lafayette, Indiana, USA

Correspondence: Pablo D. Zavattieri (zavattie@purdue.edu)

Received: 7 May 2026 | **Revised:** 13 August 2026 | **Accepted:** 23 September 2026

Keywords: 3D-printed concrete | bio-inspired desings | damage delocalization | energy absorption | impact resistance | mechanical anisotropy | non-planar Bouligand architecture

ABSTRACT

Brittle and quasi-brittle materials such as hydraulic cement-based materials, glass, and ceramics exhibit limited toughness and poor energy absorption, often leading to catastrophic failure under extreme loading. Inspired by the dactyl club of the *Mantis shrimp*, we introduce a sinusoidal Bouligand architecture into concrete enabled by nonplanar additive manufacturing. Under quasi-static compression, the elements with sinusoidal Bouligand architecture exhibit a 53.6% higher compressive strength and a 216.1% greater work of failure than regular 3D-printed elements, while also outperforming cast counterparts by 13.5% in strength and 35% in work of failure. Under impact loading, the sinusoidal Bouligand samples exhibit up to a 68.6% increase in peak load and a 49.2% increase in absorbed energy compared to cast counterparts. These improvements enable the architected samples to maintain structural integrity without catastrophic failure, whereas the cast samples fail by highly localized fracture. Fiber alignment during 3D printing induces strong and tunable local anisotropy which, coupled with the sinusoidal Bouligand architecture, enables interfacial crack deflection, crack twisting, and damage delocalization. These results demonstrate the effective translation of biological toughening principles into engineered materials and establish a design paradigm for cementitious composites with enhanced damage tolerance and energy-absorbing capability.

1 | Introduction

Brittle and quasi-brittle engineering materials (e.g., hydraulic cement-based materials, glass, and ceramics) are valued for their relatively high strength and stiffness. However, they typically exhibit low toughness and limited energy-absorption capacity. These materials can fail catastrophically under applied loading, limiting their reliability in demanding structural applications. Addressing this inherent trade-off between high strength and high toughness remains a long-standing challenge [1]. On the other hand, natural systems, despite being composed of brittle components, exhibit remarkable damage tolerance and energy absorption through nature-designed internal architecture arrangements [2–5]. The bio-inspired designs drawn from these biological systems offer a promising pathway to enhancing the toughness and energy-absorption capacity of engineering materials, and can possibly also enable emerging properties and functionalities that are challenging to achieve through conventional design approaches [6–11].

The *Mantis shrimp* provides an excellent example of bio-inspired design through its dactyl club, an organ capable of delivering

This is an open access article under the terms of the Creative Commons Attribution License, which permits use, distribution and reproduction in any medium, provided the original work is properly cited.
© 2026 The Author(s). *Advanced Materials* published by Wiley-VCH GmbH

rapid, high-force strikes without sustaining catastrophic damage [2]. The dactyl club can reach striking speeds of approximately 23 m/s, with accelerations exceeding 10 000 g, and generate impact forces of up to 1500 N, making it one of the most powerful biological impact systems known in nature [12]. The dactyl club showcases several synergistic toughening mechanisms that prevent catastrophic failure under extreme loads. As a crack initiates and propagates under applied loading, the helicoidal fiber architecture of the dactyl club, known as a Bouligand structure, consisting of stacked layers with gradually rotated orientations, forces the crack to undergo deflection and twisting, thereby absorbing energy and blunting the crack driving force [13, 14]. This crack-twisting mechanism has been reported to enhance material toughness and energy-absorption capacity [15, 16]. In addition, the sophisticated architecture of the dactyl club promotes distributed damage rather than a single catastrophic fracture [17]. The inherent local anisotropy and weak interfaces between helicoidally aligned fibers and the matrix enable microcracks to nucleate at multiple sites [16]. These microcracks help delocalize damage and dissipate impact energy over a larger volume of material, rather than concentrating it in a single catastrophic crack [16, 17]. Furthermore, the multi-regional hierarchical architecture allows stress to be regulated at multiple levels [2]. The outer layer of the dactyl club of *Mantis shrimp* is characterized by a sinusoidal Bouligand architecture, in which helicoidally stacked fiber layers with progressively rotated orientations follow a sinusoidal wave pattern and are highly effective at withstanding intense compressive loads by distributing stress and damage [18]. In contrast, the inner layers, with their planar Bouligand architecture (fiber layers arranged in a straight and planar pattern with progressively rotated orientations), withstand principal stress and dissipate impact energy through crack twisting [2]. Previous work has shown that the sinusoidal Bouligand architecture in the impact region provides superior resistance to compressive loading compared with the planar Bouligand architecture [18]. Moreover, sinusoidal architectures are widely present in biological systems, for example, in beetle *Elytra*, where they have been examined for their capacity to enhance energy absorption and fracture toughness [3, 19–21].

Inspired by the dactyl club of *Mantis shrimp*, considerable effort has been devoted to leveraging Bouligand architectures to enhance the toughness and impact resistance of engineering materials, such as ceramics [22], nano composite [12], carbon fiber–epoxy composites [23], and polymers [24]. Recent advancements in 3D-printed concrete have enabled the exploration of novel designs that enhance the mechanical performance of cement-based materials beyond what can be achieved using conventional methods [7, 25–27]. In this context, Bouligand architectures have been investigated to enhance the mechanical response of cement-based materials [7, 28–31]. However, most reported designs still rely on regular planar Bouligand configurations [32, 33] and overlook the importance of sinusoidal Bouligand architecture featured in the impact region. The superior compressive load-bearing capacity of this sinusoidal Bouligand architecture is particularly relevant to concrete, given its structural role in practical applications where compressive stresses are dominant. Besides, the influence of inherent anisotropy on achieving optimal toughening has not received sufficient direct attention. In fact, in additively manufactured concrete, anisotropy introduced by microstructural heterogeneities, including pores and interfaces, is often treated as a weakness that undermines mechanical performance, and much of the current research focuses on eliminating or strengthening these printing-induced interfaces [34–37]. Drawing inspiration from the dactyl club of *Mantis shrimp*, which leverages weak interfaces and local anisotropy to distribute damage and enhance energy absorption, we propose a shift away from this conventional view. We aim to utilize heterogeneous interfaces in combination with clever architectures to enable favorable damage mechanisms and enhance the mechanical response of inherently brittle materials.

In this study, we shift from conventional planar filament designs to nonplanar filament architectures and introduce a sinusoidal Bouligand architecture in concrete, made possible by additive manufacturing. Nonplanar printing has also been investigated in other material systems such as polymer composites [38, 39]; however, these approaches cannot be directly translated to 3D printed concrete because of their different material behavior and manufacturing constraints, including complex rheology, large extrusion nozzle sizes, fresh-state stability requirements, and gravity-induced deformation during deposition. We examine the design principles required for active *X*–*Y*–*Z* toolpath control on sinusoidal surfaces, which allows the fabrication of this complex sinusoidal Bouligand architecture. By incorporating short metal fibers into concrete, we induce strong and tunable anisotropy and combine it with clever architecture to improve its mechanical response. Mechanical investigations show that the sinusoidal Bouligand architecture provides substantial improvements in both strength and energy absorption, outperforming traditional cast elements. Finite element analysis and micro-CT were performed to understand the underlying damage and toughening mechanisms. This approach effectively translates multiscale toughening mechanisms found in nature into engineered materials, enabling superior damage tolerance and energy absorption. It further establishes a new design paradigm for concrete materials, highlighting the transformative potential of bio-inspired strategies and additive manufacturing to enable advanced characteristics that are challenging to achieve through conventional manufacturing processes.

2 | Results

Figure 1a–c shows the dactyl club of the *Mantis shrimp* and the microstructures of its impact and periodic regions. The dactyl club exhibits multi-regional architecture that is optimized to withstand extreme impact loads, with distinct regions specialized for resisting varied loading conditions [2]. The SEM image reveals that the outermost impact region features a unique sinusoidal Bouligand architecture. This architecture has been reported to enable the dactyl club to withstand high-magnitude compressive stress without structural failure by effectively distributing stress and damage [18]. Beneath this lies the periodic region, composed of helicoidally aligned fibers that form a planar Bouligand architecture. This region serves as a tough, energy-dissipating zone that absorbs energy by promoting crack twisting and damage delocalization [14].

Inspired by this natural design, we developed biomimetic concrete using an extrusion-based 3D printing process. Figure 1d,e present schematics of the Sinusoidal Bouligand and planar

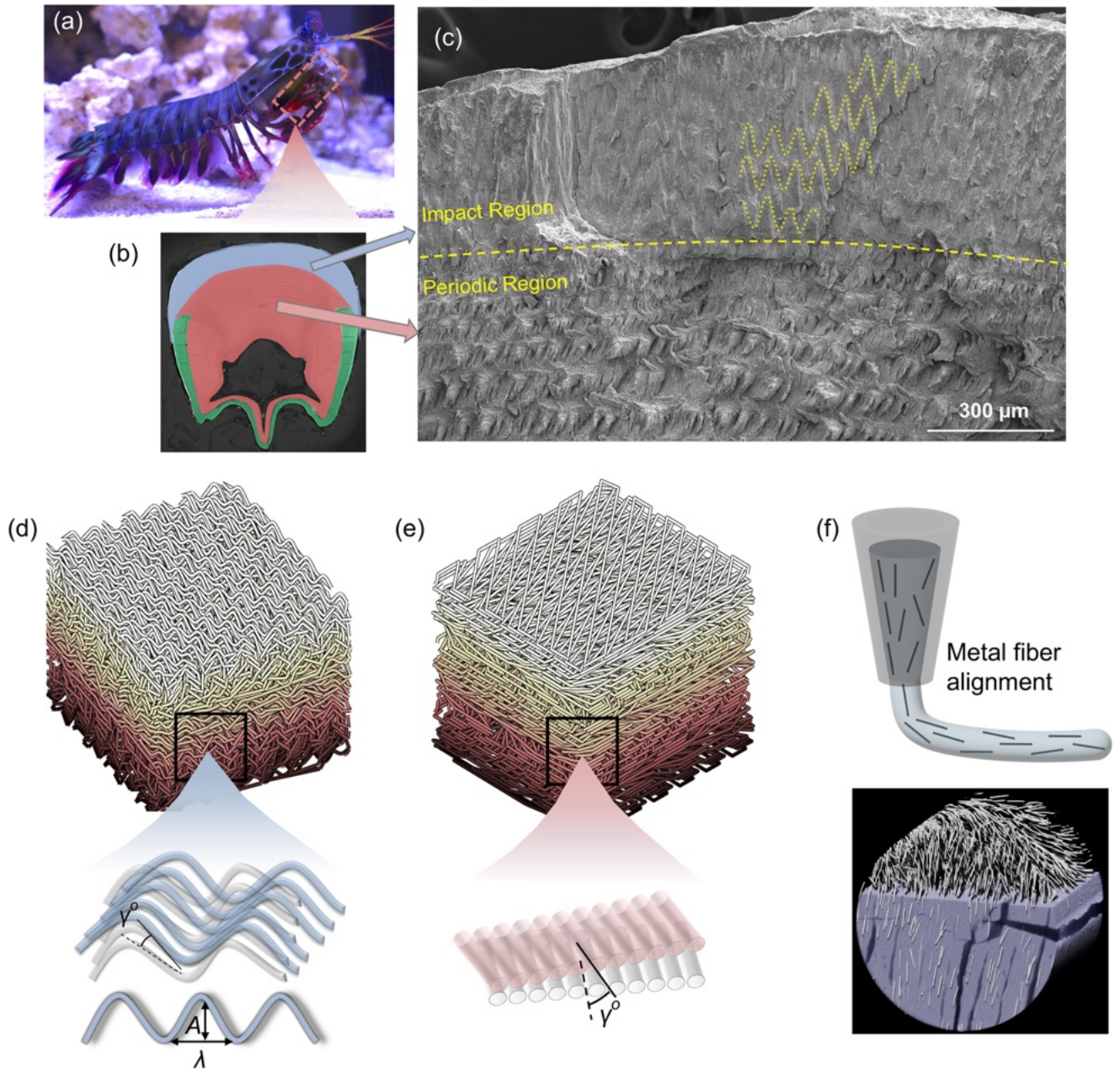


FIGURE 1 | Microstructure of the *Mantis shrimp* dactyl club and the corresponding bio-inspired architectures. (a) Photograph of a *Mantis shrimp* (photo provided by the Kisailus Biomimetics and Nanostructured Materials Lab at UC Irvine). (b) Cross-sectional view of the dactyl club of the *Mantis shrimp*. (c) SEM image showing the impact and periodic regions of the dactyl club, where the impact region features a sinusoidal architecture. Schematic illustration of (d) the sinusoidal helicoidal architecture in impact region and (e) the planar Bouligand architecture in periodic region. (f) Schematic showing the alignment of metal fibers during the filament extrusion process and CT scan showing representative fiber alignment in the planar Bouligand sample.

Bouligand architecture inspired by the microstructure of the dactyl club of *Mantis shrimp*. One of the key characteristics of these biological structures is their ability to leverage interfaces and local anisotropy to delocalize damage and enhance energy absorption. Previous bio-inspired studies in engineering materials have used continuous fiber-reinforced composites to reproduce Bouligand and sinusoidal helicoidal architectures owing to their ability to achieve highly oriented reinforcement architectures [40, 41]. However, the implementation of continuous fibers in cement-based materials remains challenging because it requires specialized fiber feeding and placement systems, especially for the manufacturing of large-scale structural elements. In contrast, short fiber-reinforced mortar is widely used in practical construction applications and is readily compatible with existing concrete manufacturing and extrusion-based printing processes. Therefore, short steel fibers were incorporated into the mortar matrix to introduce strong and tunable printing-induced anisotropy while remaining compatible with existing construction practices and extrusion-based additive manufacturing processes, facilitating scalability and practical implementation. It has been reported that during the extrusion-based 3D printing process, the fibers align preferentially along the printing direction,

resulting in pronounced mechanical anisotropy characterized by relatively strong filament and weak interfacial regions (Figure 1f) [42, 43]. This preferential fiber alignment has been demonstrated in our previous studies and other published works [43–45]. Accordingly, quantitative characterization of fiber orientation was not the primary focus of the present study and remains an important direction for future work. Instead, this work focuses on how the intrinsic anisotropy of the printed material, when combined with the proposed bio-inspired architectures, promote favorable toughening mechanisms analogous to those found in natural systems.

To achieve the sinusoidal Bouligand architecture, printing is performed on a sinusoidal surface that governs the nonplanar filament deposition. As most existing studies on 3D-printed concrete focus on planar printing with flat filament configurations, there exists limited understanding of how to reliably produce nonplanar filament architectures. To address this gap, we first examined the manufacturing process required to realize a sinusoidal filament geometry on a nonplanar surface. We developed an algorithm to systematically design printing parameters and generate G-code specifically for nonplanar 3D printing. We categorized these surfaces into four distinct types, as shown in Figure S2: (a) a regular flat surface (b) an inclined surface with single sloped gradient (Equation S1), (c) a one-dimensional (1D) sinusoidal surface (Equation S2), and (d) a two-dimensional (2D) sinusoidal surface (Equation S3). Video S1 shows the printing process on the four different surface configurations.

To achieve the desired filament shape on inclined surfaces, we conducted an experimental study examining how printing parameters influence the resulting filament geometry and aspect ratio (Figure S3a–f). The results show that upward and downward printing exhibit different deposition behaviors, resulting in differences in filament shape and stability. This analysis established relationships between the printed filament shape and key printing parameters (e.g., nozzle height, layer thickness), as well as external geometric factors that influence deposition (e.g., surface incline angle and nozzle radius), as described by Equations S5 and S6. Building on the insights gained from printing on inclined surfaces, rather than designing a toolpath that simply follows the sinusoidal profile, we developed a toolpath that incorporates two distinct regimes in downward printing and upward printing. The printing parameters are dynamically adjusted to accommodate continuous changes in the relative nozzle–surface distance caused by the varying slope along the sinusoidal curve. The results show that this two-regime toolpath preserved the sinusoidal pattern more effectively in both the overall sample geometry and the local filament shape compared to directly following the sinusoidal toolpath (Figure S4). For the detailed experimental procedure and analysis, please refer to Section S2.

Quasi-static three-point bending tests were conducted to study the influence of filament orientation and fiber volume on the flexural strength and anisotropy of 3DP samples. As shown in Figure 2a, both 90-degree specimens, with and without fibers, exhibit lower flexural strength compared to the 0° specimens. Their flexural stress–displacement curves (Figure S8a) demonstrate brittle failure, with stress dropping to zero immediately after reaching the flexural strength limit. In contrast, the flexural strength of the 0° samples increase progressively with higher fiber volume fractions. For the 0° samples with 0.5% and 1% fibers, the stress–displacement curves reveal a rapid drop in stress after reaching peak stress, but they still retain some stress resistance in the post-peak region. Furthermore, the flexural strength of the 0° sample with 1% fiber is 156.2% higher than that of the 90° sample with 1% fiber, while the 0° sample without fiber has 96.9% greater flexural strength than the 90° sample without fiber. These results highlight a notable improvement in flexural strength for the 0°-degree samples with fiber addition, while the 90° samples show no substantial enhancement. This disparity in strength improvement can be attributed to the tendency of fibers to align with the printing direction during 3D printing [42, 43]. In the 90° samples, cracks propagate along interfacial regions lacking fiber reinforcement, thereby limiting the contribution of the fibers to flexural strength. In the 0° samples, however, the fibers align perpendicular to the crack propagation direction, thereby enhancing flexural strength. These findings suggest that fiber incorporation significantly influences the anisotropic behavior of 3DP samples, and that varying fiber volume fractions can modulate this anisotropy [36, 42, 46].

Figure 2b compares the compressive strengths of cast and 3DP elements tested in different orientations. The 3D-printed elements tested along the *X* and *Y* directions exhibited similar compressive strengths, which were 16.8% and 17.7% higher, respectively, than those measured in the *Z* direction. These results reveal an anisotropic behavior in the printed samples. Furthermore, the 3DP elements demonstrated consistently lower compressive strengths than their cast counterparts across all testing directions. This reduction is attributed to weak interfacial bonding between filaments in conventionally printed elements, which facilitates catastrophic crack propagation and reduces strength (as evidenced by the DIC results of the specimen tested in *Z* direction (Figure 2b).

The results demonstrate that filament orientation influences the mechanical behavior of 3DP elements, affecting both compressive and flexural strength. The testing direction plays a crucial role in determining these responses, leading to strong anisotropic behavior. Current research in the concrete field primarily focuses on methods to strengthen interfaces and minimize the inherent anisotropy in 3DP concrete [34–36]. On the other hand, nature utilizes this anisotropy to enhance damage tolerance and energy absorption [3, 5, 47]. Previous studies have demonstrated that the dactyl club of *Mantis shrimp* contains stiff minerals and hierarchically organized fibrous architectures with pronounced local anisotropy, enabling efficient energy dissipation and enhanced mechanical performance under impact loading [15, 16]. By leveraging the inherent anisotropy of fiber-reinforced mortar in combination with innovative architectures, it is possible to significantly enhance the mechanical performance of concrete beyond that achievable with conventional approaches.

Building on the strong anisotropy and inspiration from the *Mantis shrimp*, we first evaluate the feasibility of activating the characteristic interfacial crack-twisting mechanisms of Bouligand architectures through controlled anisotropy (Section S3). Section S3 presents the detailed design of the Bouligand architecture and the associated results. Figure S7 presents a comparative analysis of crack patterns in Bouligand samples with different levels of

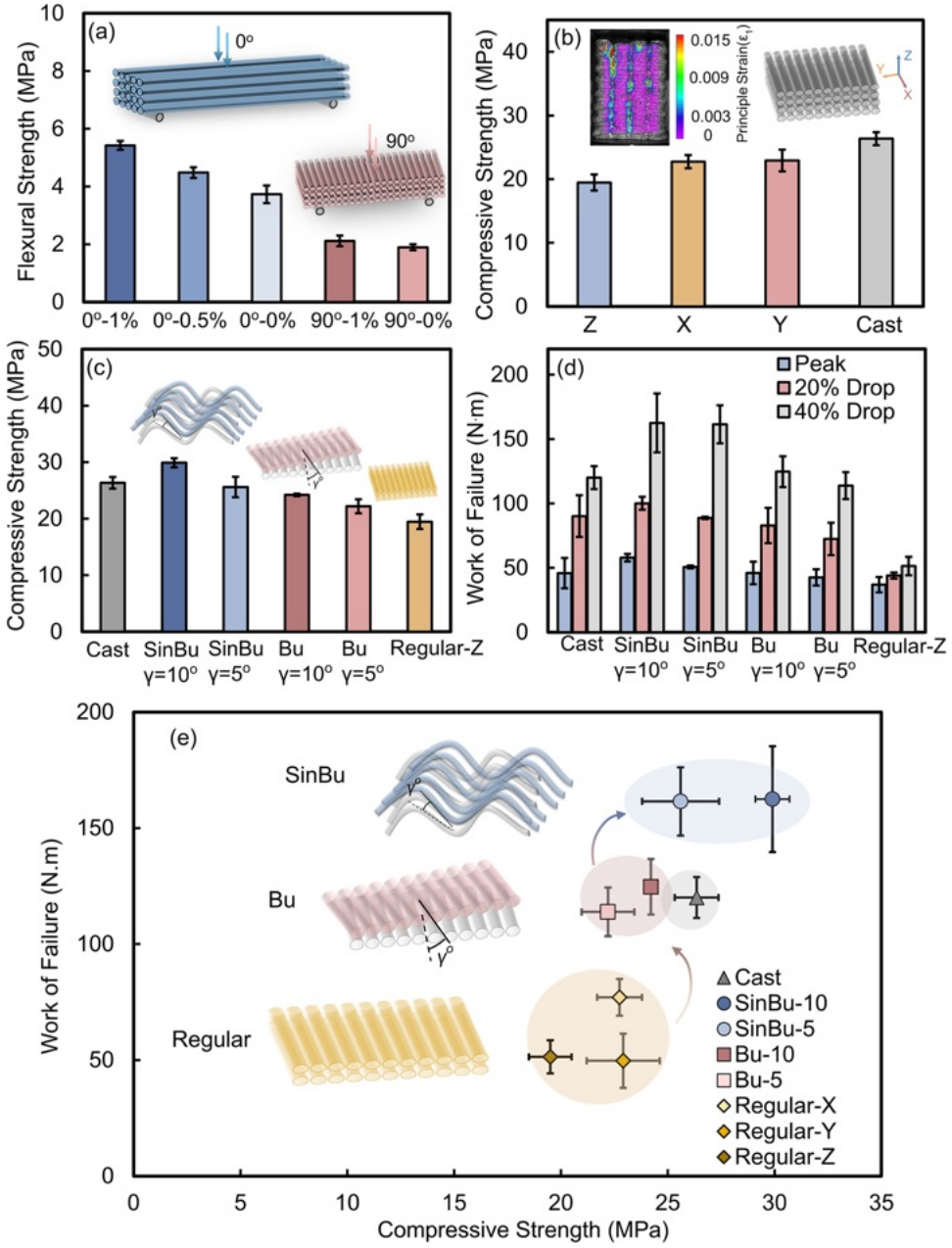


FIGURE 2 | Results of the quasi-static mechanical testing of the 3D-printed elements. (a) Three-point bending test results for 3DP samples with varying filament orientations and fiber volume fractions. (b) Compressive test results for regular 3DP samples with straight filament configurations, loaded along different directions. (c) Compressive strength and (d) Work of failure comparison across different sample configurations, including cast samples, conventionally printed straight-filament (regular) configurations, and planar Bouligand and sinusoidal helicoidal architectures with pitch angles of 5° and 10°. (e) Ashby plot comparing the compressive strength and work of failure for different configurations. Data are presented as mean ± standard deviation; error bars represent the standard deviation.

anisotropy induced by varying fiber volume fractions (1%, 0.5%, and 0%). In samples without fiber and those with 0.5% fiber (low anisotropy), crack propagated through the filaments with limited crack twisting. In these cases, the low anisotropy and lower filament strength caused cracks to develop within the filaments rather than following the intended interfacial path. In contrast, samples containing 1% fiber exhibited distinct crack patterns characterized by pronounced crack twisting along the printing interface. Figure S7e includes 3D scans of the fractured samples. The results demonstrate that cracks twisted along the interface within the tensile region below the neutral axis, following the interface along the designed toolpath. These results demonstrate that the tunable anisotropy in 3D-printed elements can be used to manipulate the fracture path, achieving behavior similar to that observed in natural structures that utilize local anisotropy to induce crack twisting.

Previous findings have shown that the sinusoidal Bouligand architecture provides superior compressive load-bearing capacity [18]. Motivated by these insights, we evaluated the behavior of architected samples featuring sinusoidal Bouligand and planar Bouligand architecture under compressive loading. In this

section, we compared the mechanical response of the non-planar sinusoidal Bouligand architecture with several configurations, including the planar Bouligand architecture, conventionally printed straight-filament (regular) specimens, and cast specimens. Figure 2c,d presents the compressive strength and work of failure (WOF) of specimens with planar Bouligand and sinusoidal Bouligand architectures featuring two pitch angles, alongside cast and straight-filament (regular) 3DP samples. The compressive strength of planar Bouligand specimens (Bu-10 and Bu-5) exceeded that of the Z-direction regular sample by 24.4% and 14.1%, respectively, while remaining 8.1% and 15.7% lower than that of the cast counterparts. The WOF, defined as the area under the load–displacement curve up to a specified damage level and representing the energy required to induce failure, shows significant increase for the planar Bouligand configurations. Specifically, Bu-10 and Bu-5 samples exhibited WOF levels comparable to cast samples and 142.5% and 121.5% larger, respectively, than the regular printed sample tested in Z-direction. With the incorporation of sinusoidal helicoidal architecture, both the compressive strength and WOF were further enhanced. Specifically, the compressive strength of SinBu-10 and SinBu-5 samples surpassed that of the *Z*-direction regular 3DP sample by 53.6% and 31.5%, respectively. Similarly, their WOF increased 216.1% and 214.0% compared to the sample with a straight-filament (regular) configuration. More importantly, SinBu-10 showed a 13.5% increase in compressive strength and a 35.4% improvement in WOF compared with the cast samples. Examining the representative load–displacement curve in Figure S8c, it becomes evident that, unlike the straight (regular 3DP) sample which exhibits a sudden stress drop after reaching the peak load, the planar Bouligand and sinusoidal Bouligand elements show a gradual post-peak load decline, indicating enhanced damage tolerance and slower crack propagation.

Ashby-type plots were used to provide a direct comparison of the trade-offs between strength and WOF for specimens with different configurations (Figure 2e). The results indicate that the regular 3DP specimens exhibits reduced compressive strength and WOF compared to the cast samples. Introduction of planar Bouligand architecture improves both compressive strength and WOF, bringing them closer to the performance of the cast samples. Further enhancement is achieved with the sinusoidal helicoidal architecture, which significantly increases both compressive strength and WOF, demonstrating an improvement compared to the cast configurations. These comparative results highlight the ability of sinusoidal Bouligand architectures to enhance compressive strength, increase energy absorption, and maintain load-bearing capacity beyond the peak stress levels. Given the inherent challenge of reduced mechanical performance in 3D-printed concrete elements, this architecture offers a promising strategy to overcome such limitations. This comparison is particularly significant because conventional 3D printing initially reduces performance relative to casting, despite imposing a more ordered filament arrangement. This reduction is consistent with the introduction of printing-induced defects, including porosity and weak inter-filament interfaces, as previously reported for 3D-printed cementitious materials [45]. The planar Bouligand architecture reverses this penalty by using these interfaces as part of the toughening mechanism, leading to substantial gains in WOF and strength relative to the regular 3DP configuration. The sinusoidal Bouligand architecture further amplifies this effect, surpassing the cast specimens in both compressive strength and WOF, demonstrating that architecture can transform printing-induced heterogeneity from a limitation into a mechanism for enhanced mechanical performance.

As the dactyl club of *Mantis shrimp* is well known for its exceptional impact resistance, drop-tower impact tests were conducted to evaluate the impact performance of the architected concrete. In this section, we compared the impact resistance of the non-planar sinusoidal Bouligand architecture with that of the regular planar Bouligand architecture, conventionally printed straight-filament (regular) specimens, and cast specimens. As shown in Figure 3a, the sinusoidal Bouligand sample demonstrated the highest peak load and energy absorption among all configurations. Two impact energy levels, 56.7 and 70.9 J, were applied to evaluate the performance of the samples under different impact energy levels. At an impact energy of 56.7 J, the sinusoidal Bouligand design outperformed the other configurations, exhibiting a peak load 34.8% higher than the regular 3D-printed sample and 52.4% higher than the cast fiber-reinforced sample, with corresponding increases of 30.0% and 18.6% in absorbed impact energy. At an impact energy of 70.9 J, the sinusoidal Bouligand architecture showed a 68.6% increase in peak load and a 49.2% increase in absorbed energy compared to the cast fiber-reinforced sample. The planar Bouligand sample generally exhibits a similar energy-absorbing capacity to the sinusoidal Bouligand sample and surpasses the cast elements, while the sinusoidal Bouligand sample demonstrates a higher peak load under impact loading. Figure 3b and Figure S10a show representative load–displacement curves for the various specimens under two impact energies of 56.7 and 70.9 J, respectively. Representative curves that reflect the typical mechanical behavior of each group are presented to maintain the clarity of the figures. The higher peak load and the more gradual post-peak load decay exhibited by the sinusoidal Bouligand and planar Bouligand samples demonstrate their improved impact resistance. In addition, neither configuration showed a reduction in stiffness, demonstrating that the improved impact performance was achieved without the expense of stiffness.

Ashby-type plots were used to enable direct comparison and reveal underlying trends in the trade-offs between peak load and absorbed energy for different designs (Figure 3c). The sinusoidal Bouligand sample exhibits the highest peak load and absorbed energy among all configurations, while the planar Bouligand sample shows slightly lower peak load but comparable absorbed energy. More importantly, both architected designs significantly outperform the cast samples. This trend is especially notable because the regular 3DP specimens again show the expected reduction in impact performance associated with printing-induced porosity and weak interfaces. In contrast, the planar Bouligand and sinusoidal Bouligand architectures convert these otherwise detrimental interfaces into controlled crack paths that promote crack deflection, distributed damage, and enhanced energy dissipation under dynamic loading. As shown in the fracture pattern after impact in Figure 3d, these architectures exhibit strong resistance to crack propagation and maintain structural integrity without undergoing catastrophic failure. In contrast, the cast samples and the regular 3D-printed samples suffer severe structural damage, fracturing into multiple pieces and failing to absorb the full impact energy. Slow-motion videos of the drop-tower impact tests for specimens with different

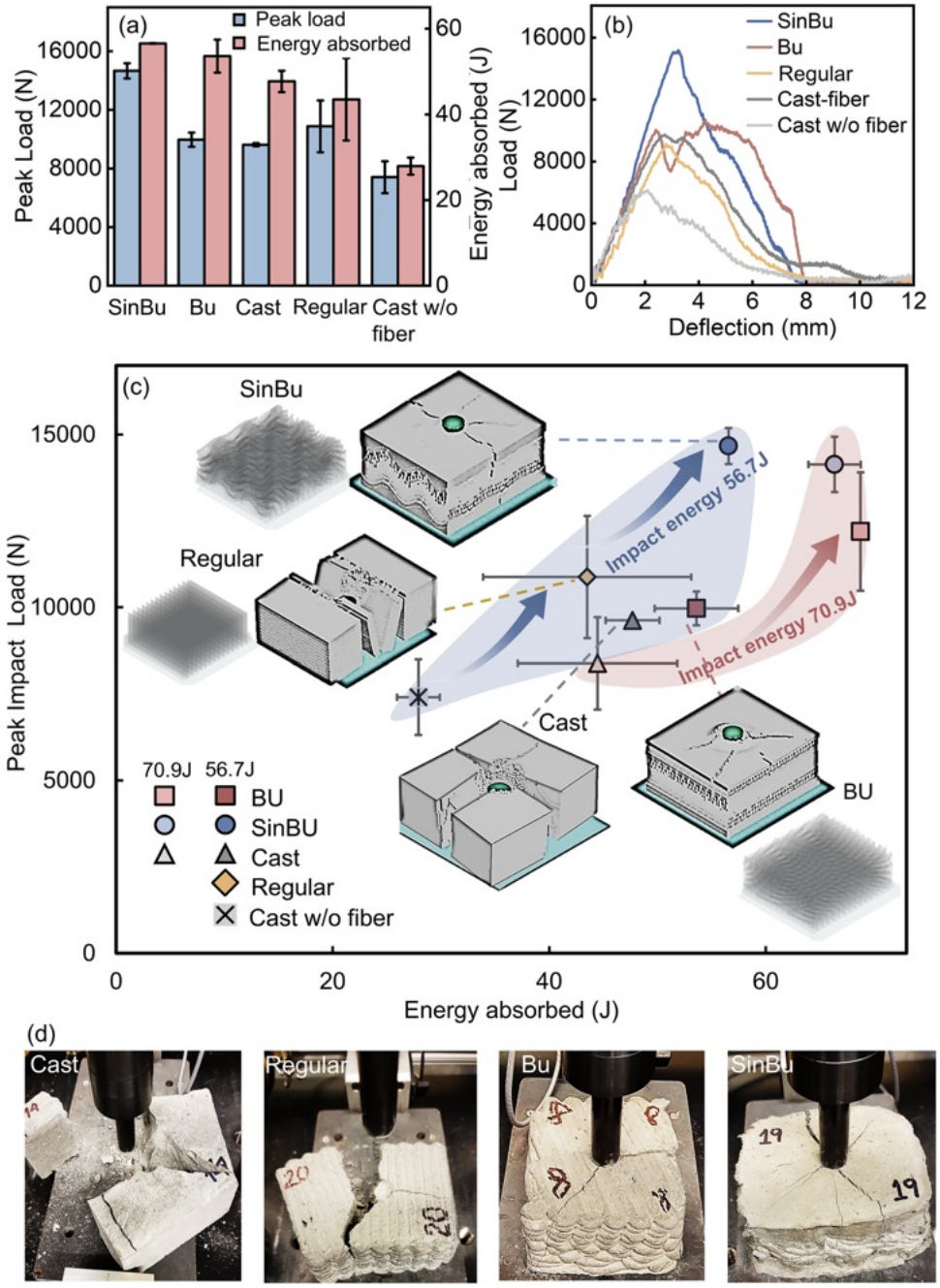


FIGURE 3 | Drop tower impact test results of different types of specimens: (a) comparison of peak load and total absorbed energy under an impact energy of 56.7 J; (b) Representative load–displacement curves from drop tower impact tests at an impact energy of 56.7 J. One representative curve from each group is shown to illustrate the typical mechanical response; (c) Ashby plot comparing peak load and absorbed energy for different types of specimens under two impact energies, 56.7 and 70.9 J; and (d) representative fracture patterns after impact for each specimen type. The cast and regular (conventionally 3D-printed) specimens fractured into multiple pieces after impact, while the planar Bouligand and sinusoidal Bouligand samples did not exhibit catastrophic failure. Data are presented as mean ± standard deviation; error bars represent the standard deviation.

configurations are provided in Video S7. The potential influence of impact location on the sinusoidal Bouligand architecture was further evaluated through finite element simulations by comparing impact at the specimen center (located between the crest and valley) and at a sinusoidal crest (Figures S43 and S44). The two loading locations exhibited similar force-displacement responses and overall damage patterns (Figures S45 and S46). These results suggest that, under the present loading configuration, the impact location has a limited influence on the global mechanical response (Section S5.4.4). These results demonstrate the enhanced impact resistance and energy-absorption capabilities of the sinusoidal Bouligand and planar Bouligand architectures. They highlight the promise of bio-inspired design for achieving performance levels that surpass those of conventionally manufactured (cast) specimens. To elucidate the observed mechanical performance, micro-CT damage analysis and finite element modeling are presented in the following section.

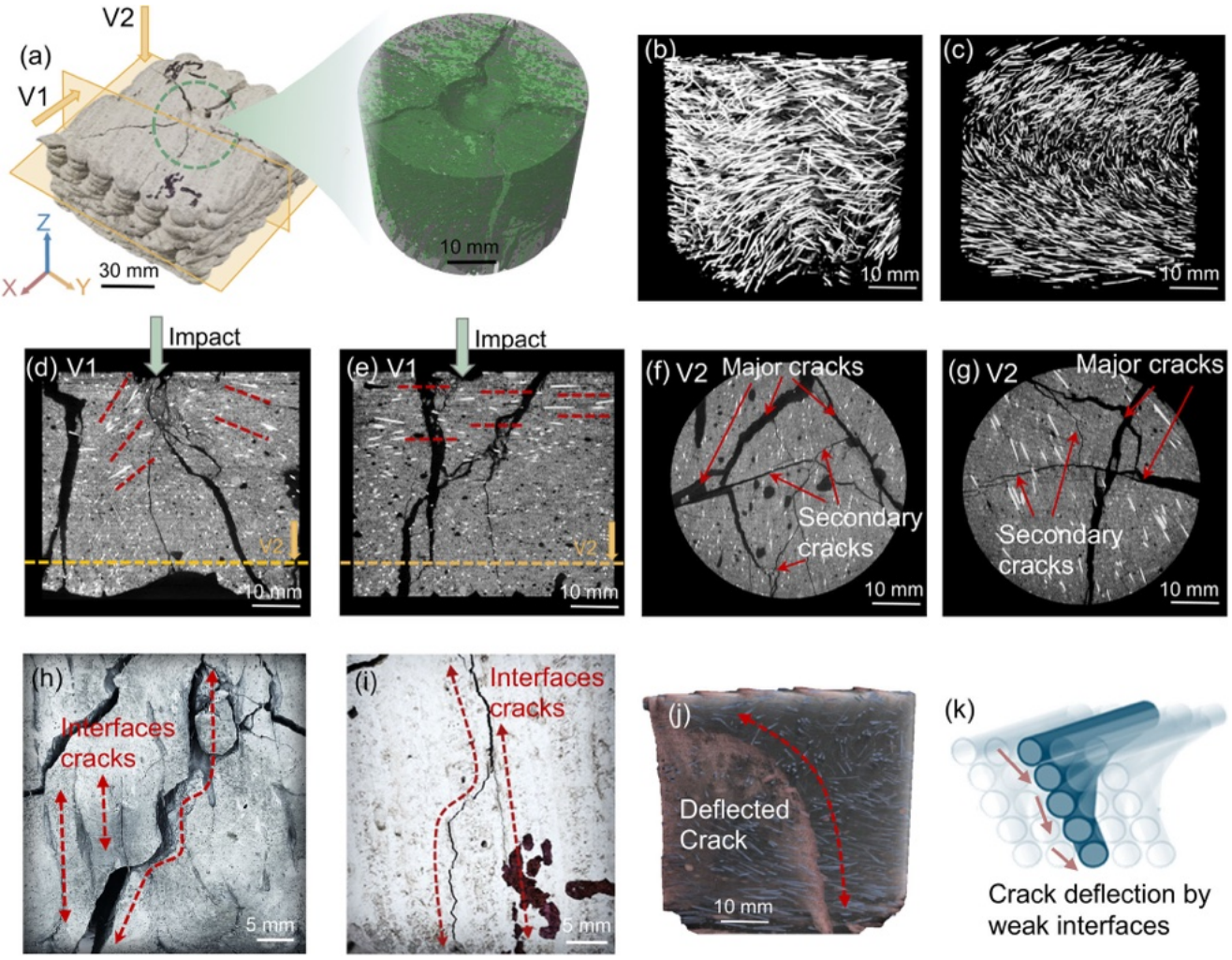


FIGURE 4 | Damage analysis of the sinusoidal Bouligand and planar Bouligand samples. (a) Example showing the region of the sample for CT scanning. 3D reconstructions of metal fiber alignment for (b) the sinusoidal Bouligand sample and (c) the planar Bouligand sample. Damage observed in different cross-sectional views: internal damage from view V1 for (d) the sinusoidal Bouligand sample and (e) the planar Bouligand sample, and from view V2 for (f) the sinusoidal Bouligand sample and (g) the planar Bouligand sample. Interfacial and deflected cracks observed on the top surfaces of the fractured (h) sinusoidal Bouligand and (i) planar Bouligand samples. (j) Representative twisted crack observed from CT scans (red regions indicate cracks). (k) Schematic illustrating the typical interfacial crack-twisting mechanisms in the Bouligand samples.

Micro-CT was performed to understand the impact-induced damage mechanisms. Figure 4a presented a representative scanned region focusing on the central portion of the specimen due to limitations of the equipment. Figure 4b,c and Video S2 present the 3D reconstructions of the metal-fiber alignment for the sinusoidal Bouligand and planar Bouligand samples, respectively. The CT images show preferential local fiber alignment consistent with the local material flow direction. In the planar Bouligand sample, the fibers exhibit a helicoidal alignment that follows the printing path. In the sinusoidal Bouligand sample, the local fiber orientation appears as a curved pattern corresponding to the local segment of the sinusoidal toolpath captured within the scanned region. These curved aligned fibers result in some fibers align in Z axis around the impact loading zone (as also shown in the cross-sectional view in Figure 4d), which may in turn provide resistance to the penetration of the impactor and enhance the ability to withstand localized impact loading. In addition, as discussed in Figure 2, preferential fiber alignment during the extrusion process strengthens the filament direction without significantly improving the strength of the interfacial regions, resulting in pronounced intrinsic anisotropy. This anisotropy, characterized by strong filaments and weak interfaces, serves as the material foundation for the proposed architected designs, where the spatially arranged weak interfaces provide preferential paths for crack propagation that redirect cracks, promote damage delocalization and distributed failure, and ultimately enhance energy absorption [14–16].

Figure 4d–k shows the damage observed in various specimens to support these observations and clarify the underlying damage mechanisms. Figure 4d–g presents internal fractures from two different cross-sectional views (V1 and V2) obtained via CT scanning. The main cracks are observed to propagate toward the bottom of the specimen along a deflected path, forming a delocalized damage pattern characterized by the presence of secondary cracks. Figure 4h,i shows interfacial cracking and crack deflection observed on the top surface of the specimen. A combination of interfacial cracks and filament cracks is observed,

with filament cracks connecting to interfacial cracks to form a deflected crack path. A 3D view of the planar Bouligand sample from CT scan further reveals a deflected crack path extending from the top to the bottom surfaces of the specimen (Figure 4j). As discussed earlier, these deflected cracks are associated with weak interfaces and local anisotropy induced by fiber alignment. During crack propagation, the crack tends to be arrested within the filaments due to fiber bridging and is redirected toward weaker regions, such as inter-filament interfaces, leading to deflected cracking and delocalized damage (Figure 4k). These observations are consistent with the established understanding of Bouligand architectures, in which crack twisting and damage delocalization arising from local anisotropy serve as key mechanisms contributing to impact resistance and enhanced energy absorption [14–16]. In addition, the local fiber-bridging effect of helicoidally aligned fibers may further enhance crack resistance within individual filaments and promote damage delocalization. An important direction for future research is the quantitative characterization of the fiber orientation distribution, orientation tensor, local fiber volume fraction, and degree of fiber alignment in different regions of the architected elements to further elucidate the damage mechanisms. Overall, these results demonstrate that the synergistic interaction between the intrinsic anisotropy of the printed material and the bio-inspired architectures is essential for activating crack twisting, damage delocalization, and enhanced energy dissipation.

Finite element modeling (FEM) was conducted to support the experimental observations and to further elucidate the damage mechanisms governing the mechanical response. The printed filaments were modeled using the MAT_159 concrete material model available in LS-Dyna, while the weaker inter-filament and interlayer interfaces were simulated using a cohesive zone model with a bilinear traction-separation law. The material properties were determined through a combination of experimental characterization, established material model parameters, and numerical calibration. Detailed descriptions of the constitutive models, parameter determination and calibration, interface modeling, mesh sensitivity analysis, and comparison between experimental and numerical results are provided in Sections S5. Figure 5a and Figures S20-S23 compare the fracture patterns of the samples after impact from the FEM simulations. Videos S3 and S4 show the fracture patterns from isometric and side views, respectively. Consistent with the experimental observations, the sinusoidal Bouligand and planar Bouligand samples exhibited improved resistance to impact loading without catastrophic failure. In contrast, the regular straight-filament sample developed catastrophic cracks along the printed interfaces, while the cast sample experienced catastrophic orthogonal cracks and split apart. Figure 5b,c and Figures S24–S29 compare the mid-sectional damage patterns and three-dimensional views of total damage. Video S5 shows the evolution of internal damage. The grey regions in Figure 5b indicate fully damaged zones represented by element deletion within the finite element simulations. The cast and regular 3D-printed samples exhibit highly localized damage originating near the impact point and propagating through the depth of the specimen. This localized fracture leads to catastrophic failure and limited energy absorption capacity. In contrast, the planar Bouligand and sinusoidal Bouligand samples exhibit smaller fully damaged regions and more distributed damage near the top portion of the specimen, with fewer major cracks extending toward the bottom. As further illustrated in Figure 5c, overall damage in these architected samples is more distributed and delocalized, whereas the cast and regular printed samples display highly concentrated damage along dominant crack paths. This distributed damage pattern suggests the formation of microcracks that dissipate energy and inhibit the growth of localized, catastrophic fractures, thereby enhancing the overall energy absorption capacity of the architected samples. Figure 5d and Figures S31–S33 present the interfacial cracks within the samples. Video S6 shows the evolution of interfacial damage. The planar Bouligand and sinusoidal Bouligand samples exhibit a twisted crack pattern along the interfaces, whereas the regular 3D-printed sample shows predominantly straight interfacial cracks. Crack deflection along the interfaces is particularly significant in the planar Bouligand and sinusoidal Bouligand samples. This twisted crack morphology, characteristic of Bouligand structures, is widely recognized for improving damage tolerance in biological materials by promoting crack deflection and inhibiting catastrophic fracture [14–16]. Figure 5e presents the energy ratio, defined as the fraction of projectile kinetic energy dissipated by the sample relative to the kinetic energy imparted to the specimen after impact. This metric reflects the ability of the material to absorb energy, resist impact without excessive motion, and maintain structural integrity. The results show that the planar Bouligand and sinusoidal Bouligand samples achieved energy ratios up to two orders of magnitude higher than those of the cast and straight -filament samples, owing to their enhanced ability to resist impact without losing structural integrity. Overall, the FEM results corroborate the experimental observations, demonstrating that distributed damage and interfacial crack twisting enabled by the planar Bouligand and sinusoidal Bouligand architectures effectively suppress catastrophic failure and effectively enhance the energy absorption.

3 | Discussions

This work introduces sinusoidal Bouligand architecture into cement-based materials through nonplanar additive manufacturing and demonstrates its ability to enhance compressive strength and energy absorption. Mechanical testing results show that the sinusoidal Bouligand design enhances performance under both quasi-static and impact loading conditions. Under quasi-static compression, the SinBu-10 sample with the sinusoidal Bouligand architecture exhibited markedly enhanced performance, with its compressive strength exceeding that of the *Z*-direction regular specimen by 53.6% and work of failure increasing by 216.1%. More importantly, the sinusoidal architecture exhibited a 13.5% higher compressive strength and a 35% greater work of failure compared to the traditional cast counterparts. Under impact loading, the architected samples achieve up to a 68.6% increase in peak load and up to a 49.2% increase in absorbed energy relative to cast elements. These improvements enable the architected specimens to effectively maintain structural integrity after impact, whereas the cast and regular 3D-printed counterparts experience catastrophic fracture. Micro-CT analyses and finite-element simulations demonstrate that interfacial crack twisting, damage delocalization, and crack arrest by fibers collectively govern the damage mechanisms. We propose that the strong and tunable local anisotropy induced during the printing process, characterized by strong filaments and relatively weak,

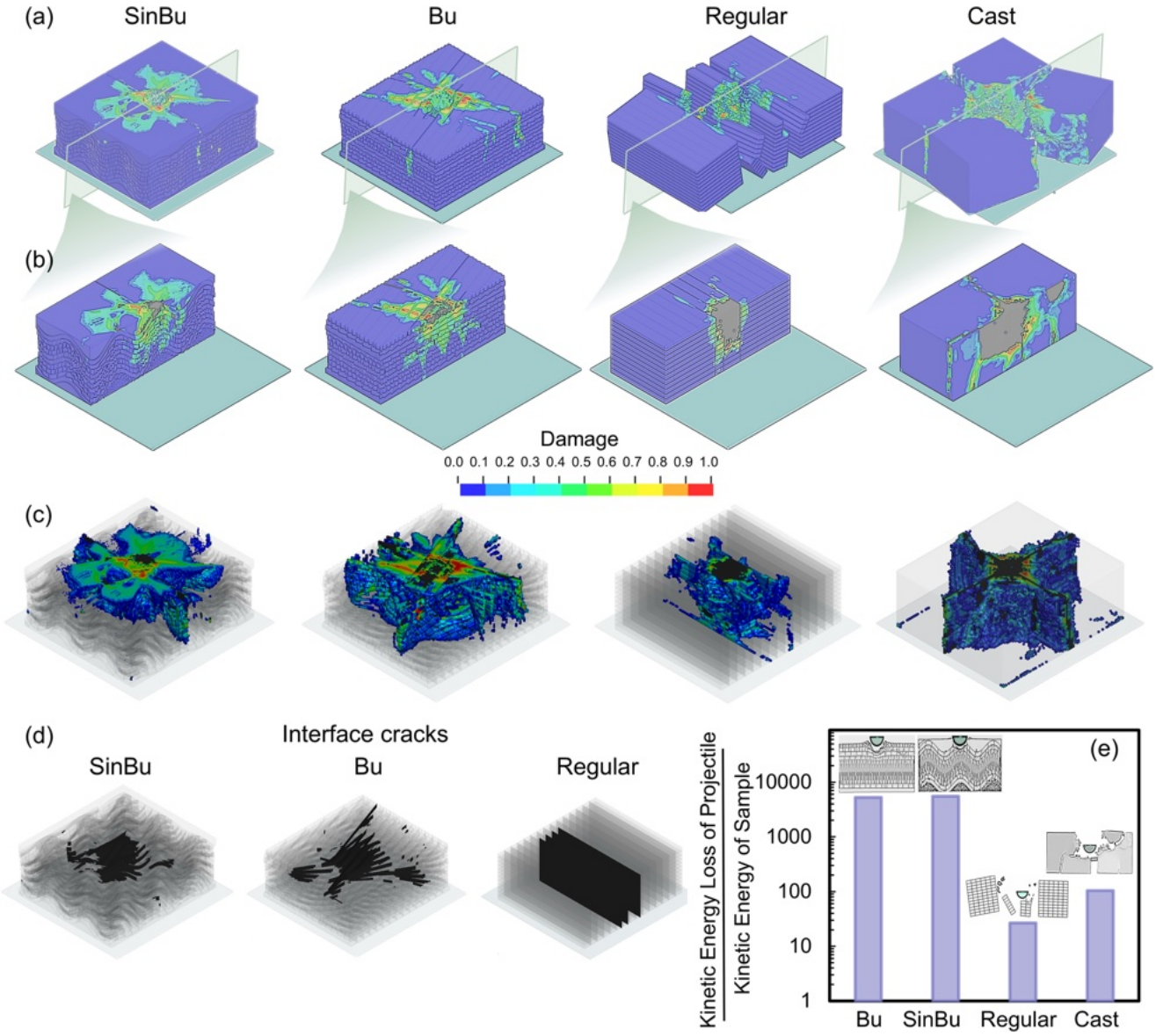


FIGURE 5 | Damage analysis from finite element modeling. (a) comparison of fracture patterns for different elements after impact; (b) cross-sectional views of internal damage, where the grey regions represent fully damaged and deleted elements (undeformed views are shown to visualize the extent of the damage); (c) comparison of the total internal damage (black regions represent fully damaged areas); (d) comparison of interfacial damage in the 3D-printed elements; and (e) comparison of the ratio of projectile kinetic energy loss and the impact-induced kinetic energy imparted to the sample, reflecting the fraction of the projectile energy absorbed relative to the kinetic energy transferred to the sample.

heterogeneous interfaces, provides the material foundation for the proposed bio-inspired architectures to promote interfacial cracking, crack twisting, damage delocalization, and enhanced energy dissipation. In extrusion-based additive manufacturing of concrete, these printing-induced weak interfaces are generally regarded as detrimental defects, and considerable research has focused on minimizing their effects or strengthening the interfacial bonding [34–36, 48]. In contrast, the present work demonstrates that these intrinsic weak interfaces can be deliberately exploited through bio-inspired architected designs. The weak interfaces within the architectures redirect crack propagation, transforming these intrinsically weak regions into structural features that promote crack twisting, damage delocalization, and therefore enhance energy dissipation. This design philosophy is consistent with previous studies showing that defects and heterogeneities can actively contribute to toughening mechanisms when incorporated into bio-inspired helicoidal architectures [22, 40].

The present study demonstrates the feasibility of fabricating non-planar sinusoidal Bouligand architectures to improve the strength and impact resistance of extrusion-based 3D-printed fiber-reinforced mortar. The proposed approach primarily involves modifying the printing toolpath and is therefore compatible with existing extrusion-based additive manufacturing systems, making it readily adaptable to the fabrication of larger structural elements. During the scaling process, however, several engineering considerations may require further investigation. The continuous three-dimensional nozzle motion may require more complex toolpath planning and more accurate control of the nozzle

position to maintain a desired nozzle–surface distance over complex geometries. At larger build heights, gravity-induced deformation and accumulated geometric deviations may reduce layer stability and geometric fidelity, thereby affecting dimensional accuracy. In addition, processing parameters such as nozzle height, layer thickness, and gravity-induced deformation during deposition may influence fiber orientation and interfacial characteristics, thereby affecting the intrinsic anisotropy of the printed material and the resulting toughening mechanisms. Further quantitative characterization of these processing–structure relationships at larger scales will facilitate the implementation of the proposed printing strategy in construction-scale applications and improve the mechanistic understanding of processing-induced anisotropy in large-scale printed structures. Nevertheless, this study establishes the design methodology and manufacturing strategy for nonplanar Sinusoidal Bouligand architectures and demonstrates their effectiveness in enhancing the mechanical performance of extrusion-based 3D-printed fiber-reinforced mortar, thereby providing a foundation for future development and large-scale implementation.

Beyond cementitious materials, the proposed nonplanar printing strategy has the potential to be applied to a broad range of extrusion-based material systems, such as polymer composites, fiber-reinforced polymers, and ceramic pastes. This broad applicability arises because the strategy primarily relies on nonplanar toolpath design rather than material-specific hardware modifications. While the specific implementation will depend on the rheological behavior and processing characteristics of each material, nonplanar toolpaths provide a general strategy for tailoring reinforcement orientation, interfacial interactions, crack propagation, and ultimately the mechanical performance of architected materials.

Overall, this work establishes a new design paradigm for concrete materials, enabling inherently brittle systems to achieve improved damage tolerance and energy-absorbing capability. More broadly, this study provides a pathway for imparting enhanced mechanical performance to emerging properties in brittle and quasi-brittle materials through architected designs inspired by biological toughening mechanisms—capabilities that are otherwise difficult to achieve using conventional manufacturing methods.

4 | Experimental Section

4.1 | Materials Formulation

The material composition was based on previous studies assessing the printability and pumpability of the concrete [49, 50]. The fresh-state properties of the mortar were tailored to provide sufficient cohesiveness and viscosity to suspend the fibers and minimize segregation during material handling and extrusion. Type IL Portland cement (Buzzi Unicem USA) and natural siliceous sand with a maximum particle size of 0.6 mm was used in this study. Supplementary cementitious materials are typically used as a sustainable and effective way to modify the fresh properties of the mixture [51]. In this study, silica fume (MasterLife SF 100) was used to replace 20% of the cement to improve the printability and buildability of the mixture. A viscosity-modifying admixture (VMA, MasterMatrix 362) was incorporated to reduce bleeding and improve ink consistency [42]. Steel fibers supplied by HiPer Fiber Inc., with a length of 5 mm and a diameter of 0.2 mm, were used in the mixture. The water, silica fume, fine aggregate, and VMA contents (dry weight) were calculated as weight percentages relative to the total binder mass (cement and silica fume). Fibers were added based on the volume of the plain mixture (without fibers). For the compressive and impact tests, the fiber volume fraction was maintained at 0.8 vol%. For the flexural tests, elements with different fiber volume fractions were evaluated to examine the influence of fiber content on flexural strength and anisotropic behavior. The proportions of the mortar mixtures used in the study are given in Table 1

4.2 | Mixing Procedure

The liquid components (water and VMA) were manually mixed in a plastic container until a homogeneous blend was achieved. The solid materials (cement, sand, and silica fume) were measured and blended in a Hobart N50 mixer at medium speed (281RPM) for two minutes. The pre-mixed liquid materials were then added, and the mixture was mixed for an additional two minutes at medium speed. After the mortar achieved a uniform consistency, the fibers were gradually incorporated into the mixture, while operating the mixer at medium speed. Following fiber integration, the mortar was mixed for five more minutes at high speed (580 RPM) to ensure proper fiber dispersion. The prolonged mixing procedure was adopted to promote uniform fiber dispersion while minimizing fiber agglomeration.

4.3 | 3D Printing

3D printing was conducted using a Hydra 16A system equipped with a 150 cm^3 plastic syringe featuring a 5.5 mm diameter opening, which served as the printing head (Figure S1). For Bouligand and other regular configurations, Simplify3D was used to generate the corresponding G-code. A MATLAB code was developed to generate the G-code for the sinusoidal Bouligand architecture, enabling customized nonplanar toolpaths. The sinusoidal Bouligand architecture was fabricated on a base with a sinusoidal profile. Further details of the 3D printing process are provided in Supplementary Material Section S1.

4.4 | Flexural Test

A three-point bending test was conducted to evaluate the flexural strength of prism specimens with varying filament orientations and fiber volume fractions. The prisms used in this study measured 35 mm × 36 mm × 170 mm. After printing, samples were air-cured in the laboratory for approximately 2 h and were subsequently transferred to a curing chamber maintained at a relative humidity of 98% ± 2% and a temperature of 23°C ± 2°C. All specimens were tested at the age of 72 ± 3 h. Testing was performed with a constant span length of 150 mm using a universal testing machine (MTS Insight 10) with a 10 kN capacity. A displacement-controlled loading rate of 0.1 mm/min was applied. Load and mid-span displacement were recorded, and

TABLE 1 | Proportions of mortar mixtures.

Water/Cem. (W/C)[a]	Sand/Cem. (S/C)[a]	Silica fume (%)[a]	VMA (%)[a]	Fibers (vol%)[b]
0.42	0.25	20	0.05	Variable

[a]With respect to the weight of total cementitious material.
[b]Percentage of the volume of the plain (no fibers) mixture.

the peak load was used to calculate the flexural strength. At least three replicate tests were conducted for each group.

4.5 | Compressive Test

Specimens used for the compressive tests had nominal dimensions of 50 mm in the X direction, 72 mm in the Y direction, and 64 mm in the Z direction (Figure S9). These dimensions were selected to ensure that the sinusoidal architecture contained two complete periods of the filament waveform, while also limiting specimen size to enable efficient fabrication using three syringe loads. For specimens tested in the X and Y directions, samples were initially printed with slightly larger dimensions and subsequently cut to the target size (50 mm × 72 mm × 64 mm) to ensure smooth and parallel loading surfaces. In contrast, specimens tested along the Z direction, exhibited sufficiently smooth as-printed surfaces and did not require post-processing prior to testing. The sinusoidal Bouligand specimens were similarly trimmed to the target dimensions prior to testing to ensure smooth and parallel loading surfaces. After printing, all specimens were air-cured in the laboratory for approximately two hours, followed by curing in a chamber maintained at a relative humidity of 98% ± 2% and a temperature of 23°C ± 2°C. Testing was conducted at an age of 72 ± 3 h. Compressive tests were performed using a universal testing machine (MTS Insight 300) with a 300 kN capacity, operated at a constant displacement rate of 0.25 mm/min. The peak load was recorded to evaluate the compressive strength, and the load–displacement curve was used to calculate the work of failure (WOF). Specifically, WOF was computed as the area under the load–displacement curve up to a specified level of post-peak damage, representing the energy required to induce failure of the sample. In this study, WOF was calculated as the area under the load–displacement curve corresponding to 0%, 20%, and 40% reductions from the peak load. At least three replicate tests were conducted for each group.

4.6 | Impact Test

For impact testing, all specimens measured 80 mm (X) × 90 mm (Y) × 36 mm (Z). For samples featuring sinusoidal helicoidal architecture, achieving smooth testing surfaces via saw cutting was challenging due to the relatively low width-to-depth ratio. Directly testing specimens with a wavy surface under impact loading could introduce local stress concentrations at the surface peaks, causing the measured response to be influenced by local contact conditions rather than primarily reflecting the global structural response. To address this, a thin layer of mortar was applied to the top and bottom surfaces to obtain smooth and parallel testing faces approximately 18 h after printing. To maintain consistent final sample height across all specimens, the sinusoidal helicoidal samples were printed with two fewer layers compared to the other configurations. The specimens were cured under the same environmental conditions as those used for the quasi-static tests for total 48 ± 2 h after printing prior to impact testing. The impact location was consistently positioned at the center of every specimen for all experimental groups to ensure identical loading conditions and enable consistent comparisons among the different architectures. Impact tests were conducted using an Instron drop tower, equipped with a 15 mm diameter hemispherical-tip impactor and a 7.231 kg drop weight. The sample was placed on a solid metal plate without boundary constraints. Two impact energy levels were applied: 56.7 J (corresponding to a drop height of 0.8 m) and 70.9 J (corresponding to a drop height of 1 m). During testing, load–displacement curves were recorded, and the impact events were recorded using a slow-motion camera. At least two replicate tests were conducted for each group.

4.7 | Micro-CT Characterization

X-ray computed tomography (CT) scans were performed using a Zeiss Xradia 510 Versa. Due to size constraints, only the central region of each specimen, with an approximate diameter of 50 mm, was scanned. All scans were conducted at 150 kV and 10 W, resulting in a spatial resolution of 46–48 μm. Three-dimensional reconstruction and quantitative analysis of damage patterns and fiber orientation were performed using Dragonfly Pro software.

4.8 | Finite Element Modeling

Finite element simulations were performed using the commercial software ANSYS/LS-DYNA. Four configurations were considered: cast, planar Bouligand, sinusoidal Bouligand, and straight-printed structures. The finite element models were developed using LS-PrePost. Concrete behavior was modeled using the widely adopted plasticity–damage constitutive model MAT_159 available in LS-DYNA [52]. The interfaces between filaments and between printed layers were modeled using a cohesive zone model, which is commonly used to simulate fracture behavior in concrete and to capture crack initiation and propagation along interfaces [53, 54]. Detailed descriptions of the constitutive models, parameter determination and calibration, interface modeling, mesh sensitivity analysis, and comparison between experimental and numerical results are provided in Sections S5.

Author Contributions

Yu Wang: formal analysis, visualization, writing – original draft, investigation, methodology, writing – review and editing, software, and

validation. **Loukham Shyamsunder**: formal analysis, visualization, writing – original draft, methodology, writing – review and editing, software, and validation. **Phani Saketh Dasika**: data curation, visualization, and methodology. **Andrew Nguyen**: visualization, investigation, and data curation. **David Kisailus**: conceptualization, formal analysis, writing – review and editing, and investigation. **Jan Olek**: conceptualization, formal analysis, writing – review and editing, funding acquisition, supervision, and resources. **Jeffrey P. Youngblood**: conceptualization, formal analysis, writing – review and editing, funding acquisition, supervision, and resources. **Pablo D. Zavattieri**: conceptualization, formal analysis, visualization, writing – original draft, methodology, supervision, writing – review and editing, validation, funding acquisition, and resources.

Acknowledgements

The authors acknowledge the generous support for this research from the Transportation Infrastructure Precast Innovation Center (TRANS-IPIC) through award PU-23-RP-03, the Center for Durable and Resilient Transportation Infrastructure (DuRe-Transp) through the grant 69A3552348339, subaward No. 2022GC4889: the NSF Small Business Technology Transfer (STTR) Phase II program through award #2333306, and the NSF AccelNet program granted to Purdue University through award #2020095. P.D.Z. and D.K. wish to acknowledge financial support from the Air Force Office of Scientific Research (AFOSR-FA9550-23-1-0209) and the Multi-University Research Initiative (AFOSR-FA9550–15–1–0009). D.K. gratefully acknowledges support from a JSPS Fellowship (Fellowship ID L26554) from the Japan Society for the Promotion of Science, and the Institute of Global Innovation Research, Tokyo University of Agriculture and Technology. The authors also acknowledge resources and support from the Pankow Materials Laboratory and the Chemical Laboratory at Purdue University. The authors acknowledge the 3D X-Ray Microscope Facility in the Department of Physics for CT scan results shown in this paper, which were acquired on a Zeiss Xradia 510 Versa 3D X-ray Microscope that was supported by the EVPRP Major Multi-User Equipment Program 2017 at Purdue University. The authors thank Dr. Zherui Martinez-Guo for providing access to the impact testing equipment used in this study, and Dr. Waterloo Tsutsui for assistance, guidance, and valuable discussions related to the impact testing.

Conflicts of Interest

The authors declare no conflicts of interest.

Data Availability Statement

The data that support the findings of this study are available from the corresponding author upon reasonable request.

References

1. R. O. Ritchie, "The Conflicts Between Strength and Toughness," *Nature Materials* 10 (2011): 817–822.

2. J. C. Weaver, G. W. Milliron, A. Miserez, et al., "The Stomatopod Dactyl Club: A Formidable Damage-Tolerant Biological Hammer," *Science* 336 (2012): 1275–1280.

3. J. Rivera, M. S. Hosseini, D. Restrepo, et al., "Toughening Mechanisms of the *Elytra* of the Diabolical Ironclad Beetle," *Nature* 586 (2020): 543–548, https://doi.org/10.1038/s41586-020-2813-8.

4. N. A. Alderete, S. Sandeep, S. Raetz, M. Asgari, M. A. Ghanem, and H. D. Espinosa, "Does the *Mantis shrimp* Pack a Phononic Shield?," *Science* 387 (2025): 659–666.

5. F. Barthelat, H. Tang, P. D. Zavattieri, C. M. Li, and H. D. Espinosa, "On the Mechanics of Mother-of-Pearl: A Key Feature in the Material Hierarchical Structure," *Journal of the Mechanics and Physics of Solids* 55 (2007): 306–337, https://doi.org/10.1016/j.jmps.2006.07.007.

6. H. D. Espinosa, A. L. Juster, F. J. Latourte, O. Y. Loh, D. Gregoire, and P. D. Zavattieri, "Tablet-Level Origin of Toughening in Abalone Shells and Translation to Synthetic Composite Materials," *Nature Communications* 2 (2011): 173, https://doi.org/10.1038/ncomms1172.

7. M. Moini, J. Olek, J. P. Youngblood, B. Magee, and P. D. Zavattieri, "Additive Manufacturing and Performance of Architectured Cement-Based Materials," *Advanced Materials* 30 (2018): 1802123, https://doi.org/10.1002/adma.201802123.

8. U. G. K. Wegst, H. Bai, E. Saiz, A. P. Tomsia, and R. O. Ritchie, "Bioinspired Structural Materials," *Nature Materials* 14 (2014): 23–36, https://doi.org/10.1038/nmat4089.

9. Z. Wu, H. Pan, P. Huang, J. Tang, and W. She, "Biomimetic Mechanical Robust Cement–Resin Composites With Machine Learning-Assisted Gradient Hierarchical Structures," *Advanced Materials* 36 (2024): 2405183, https://doi.org/10.1002/adma.202405183.

10. P. S. Dasika, Y. Zhang, T. N. Sullivan, S. Tavares, M. A. Meyers, and P. D. Zavattieri, "Mechanistic Insights Into hydration-Driven Shape Memory Response in Keratinous Avian Feather Structures," *Acta Biomaterialia* 195 (2025): 144–156, https://doi.org/10.1016/j.actbio.2025.02.017.

11. D. Montroni, E. Sarmiento, R. Zhao, et al., "The Multiphasic Teeth of Chiton Articulatus, an Abrasion-Resistant and Self-Sharpening Tool for Hard Algae Collection," *Advanced Functional Materials* 34 (2024): 2401658, https://doi.org/10.1002/adfm.202401658.

12. W. Huang, M. Shishehbor, N. Guarín-Zapata, et al., "A Natural Impact-Resistant Bicontinuous Composite Nanoparticle Coating," *Nature Materials* 19 (2020): 1236–1243, https://doi.org/10.1038/s41563-020-0768-7.

13. P. D. Zavattieri, "Naturally Twisted to Sieve Stress," *Science* 387 (2025): 578–579.

14. N. Suksangpanya, N. A. Yaraghi, D. Kisailus, and P. Zavattieri, "Twisting Cracks in Bouligand Structures," *Journal of the Mechanical Behavior of Biomedical Materials* 76 (2017): 38–57, https://doi.org/10.1016/j.jmbbm.2017.06.010.

15. N. Suksangpanya, N. A. Yaraghi, R. B. Pipes, D. Kisailus, and P. Zavattieri, "Crack Twisting and Toughening Strategies in Bouligand Architectures," *International Journal of Solids and Structures* 150 (2018): 83–106, https://doi.org/10.1016/j.ijsolstr.2018.06.004.

16. A. Garnica, E. Aparicio, M. Shishehbor, D. Kisailus, E. M. Bringa, and P. D. Zavattieri, "How Crack Twisting in Bouligand Structures Lead to Damage Delocalization and Toughening," *Extreme Mechanics Letters* 71 (2024): 102190, https://doi.org/10.1016/j.eml.2024.102190.

17. W. Huang, D. Restrepo, J. Y. Jung, et al., "Multiscale Toughening Mechanisms in Biological Materials and Bioinspired Designs," *Advanced Materials* 31 (2019): 1901561, https://doi.org/10.1002/adma.201901561.

18. N. A. Yaraghi, N. Guarín-Zapata, L. K. Grunenfelder, et al., "A Sinusoidally Architected Helicoidal Biocomposite," *Advanced Materials* 28 (2016): 6835–6844, https://doi.org/10.1002/adma.201600786.

19. J. Zhou, M. Zou, B. F. Ng, and M. Ou, "Emerging Sinusoidal Structures for Energy Absorption: Mechanisms, Optimizations and Applications," *Composites Part B: Engineering* 306 (2025): 112759, https://doi.org/10.1016/j.compositesb.2025.112759.

20. Y. Wang, O. Quintero, J. A. Mesa, J. Bris, and P. Zavattieri, "Fracture and Fatigue Behavior of Sinusoidal Interface Adhesive Joints Using a Modified Double Cantilever Beam Geometry," *Engineering Fracture Mechanics* 332 (2026): 111746, https://doi.org/10.1016/j.engfracmech.2025.111746.

21. A. Prihar, M. E. M. Garlock, A. Najmeddine, and R. Moini, "Mechanical Performance of Sinusoidally Architected Concrete Enabled by Robotic Additive Manufacturing," *Materials and Design* 238 (2024): 112671, https://doi.org/10.1016/j.matdes.2024.112671.

22. S. M. Wen, S. M. Chen, W. Gao, et al., "Biomimetic Gradient Bouligand Structure Enhances Impact Resistance of Ceramic–Polymer Composites," *Advanced Materials* 35 (2023): 2211175, https://doi.org/10.1002/adma.202211175.

23. L. K. Grunenfelder, N. Suksangpanya, C. Salinas, et al., "Bio-Inspired Impact-Resistant Composites," *Acta Biomaterialia* 10 (2014): 3997–4008, https://doi.org/10.1016/j.actbio.2014.03.022.

24. S. M. Wen, W. Gao, S. C. Zhang, et al., "Gradient Double-Twisted Bouligand Structural Design for High Impact Resistance Over a Wide Range Of Loading Velocities," *Science Advances* 11 (2025): 2169, https://doi.org/10.1126/sciadv.adv2169.

25. Y. Wang, A. E. Douba, N. Rajendiran, et al., "Cellulose Nanofibers and Limestone Filler Enable High-Performance, Sustainable, and Cost-Efficient Printable Concrete," *Nature Communications* 17 (2026): 3481, https://doi.org/10.1038/s41467-026-69373-5.

26. G. Du, X. Deng, and Y. Qian, "Biomimetic 3D Printed Herringbone-Bouligand SHCC for Ultra-High Impact Resistance," *Composites Part B: Engineering* 308 (2026): 112993, https://doi.org/10.1016/j.compositesb.2025.112993.

27. S. Li, Y. Sun, Y. Qian, W. Chen, J. Hu, and X. Yu, "Optimizing Mechanical Performance of Strain-Hardening Cementitious Composite Joints Using Bio-Inspired Structured Suture Interfaces With Geometrically-Tuned Deformation," *Engineering Fracture Mechanics* 339 (2026): 112097, https://doi.org/10.1016/j.engfracmech.2026.112097.

28. A. Prihar, S. Gupta, H. S. Esmaeeli, and R. Moini, "Tough Double-Bouligand Architected Concrete Enabled by Robotic Additive Manufacturing," *Nature Communications* 15 (2024): 7498, https://doi.org/10.1038/s41467-024-51640-y.

29. G. Du, Y. Sun, and Y. Qian, "Flexural Performance of Nature-Inspired 3D-Printed Strain-Hardening Cementitious Composites (3DP-SHCC) With Bouligand Structures," *Cement and Concrete Composites* 149 (2024): 105494, https://doi.org/10.1016/j.cemconcomp.2024.105494.

30. K. Xia, Y. chen, Y. Chen, L. Jia, Z. Jia, and Y. Zhang, "Programmable Toughening for 3D Printed Concrete and Architected Cementitious Materials," *Composites Part B: Engineering* 303 (2025): 112573, https://doi.org/10.1016/j.compositesb.2025.112573.

31. J. Liu, S. Li, K. Fox, and P. Tran, "3D Concrete Printing of Bioinspired Bouligand Structure: A Study on Impact Resistance," *Additive Manufacturing* 50 (2022): 102544.

32. S. Li, Y. Sun, D. Zhang, et al., "Bio-Inspired Bouligand Architectures Enable Biaxial Toughening and Programmable Energy Dissipation in 3D-Printed Strain-Hardening Cementitious Composites," *Cement and Concrete Composites* 171 (2026): 106597, https://doi.org/10.1016/j.cemconcomp.2026.106597.

33. S. Li, Y. Sun, Y. Qian, W. Chen, D. Zhang, and X. Yu, "Bio-Inspired Bouligand Architectures for Enhanced Flexural Performance in 3D-Printed Strain-hardening Cementitious Composites (3DP-SHCC)," *Composites Part B: Engineering* 307 (2025): 112922, https://doi.org/10.1016/j.compositesb.2025.112922.

34. W. Zhou, W. McGee, H. S. Gökçe, and V. C. Li, "A Bio-Inspired Solution to Alleviate Anisotropy of 3D Printed Engineered Cementitious Composites (3DP-ECC): Knitting/Tilting Filaments," *Automation in Construction* 155 (2023): 105051, https://doi.org/10.1016/j.autcon.2023.105051.

35. Q. Jiang, Q. Liu, S. Wu, H. Zheng, and W. Sun, "Modification Effect of Nanosilica and Polypropylene Fiber for Extrusion-Based 3D Printing Concrete: Printability and Mechanical Anisotropy," *Additive Manufacturing* 56 (2022): 102944.

36. Y. Yang, C. Wu, Z. Liu, H. Wang, and Q. Ren, "Mechanical Anisotropy of Ultra-High Performance Fibre-Reinforced Concrete for 3D Printing," *Cement and Concrete Composites* 125 (2022): 104310, https://doi.org/10.1016/j.cemconcomp.2021.104310.

37. M. Salmi, O. Sucharda, J. Akmal, S. Surehali, A. Tripathi, and N. Neithalath, "Anisotropy in Additively Manufactured Concrete Specimens Under Compressive Loading—Quantification of the Effects of Layer Height and Fiber Reinforcement," *Materials* 16 (2023): 5488.

38. J. Allum, J. Kitzinger, Y. Li, V. V. Silberschmidt, and A. Gleadall, "ZigZagZ: Improving Mechanical Performance in Extrusion Additive Manufacturing by Nonplanar Toolpaths," *Additive Manufacturing* 38 (2021): 101715.

39. G. A. Nisja, A. Cao, and C. Gao, "Short Review of Nonplanar Fused Deposition Modeling Printing," *Material Design & Processing Communications* 3 (2021): 221, https://doi.org/10.1002/mdp2.221.

40. S. Yin, H. Chen, R. Yang, et al., "Tough Nature-Inspired Helicoidal Composites With Printing-Induced Voids," *Cell Reports Physical Science* 1 (2020): 100109, https://doi.org/10.1016/j.xcrp.2020.100109.

41. R. Yang, H. Wang, B. Wang, S. Zhang, Z. Huang, and S. Yin, "Sinusoidally Architected Helicoidal Composites Inspired by the Dactyl Club Of *Mantis shrimp*," *International Journal of Smart and Nano Materials* 14 (2023): 321–336, https://doi.org/10.1080/19475411.2023.2236572.

42. Y. Wang, F. B. Rodriguez, J. Olek, P. D. Zavattieri, and J. P. Youngblood, "Influence of Type of Fibers on Fresh and Hardened Properties of Three-Dimensional-Printed Cementitious Mortars," *ACI Materials Journal* 121 (2024): 31.

43. A. R. Arunothayan, B. Nematollahi, R. Ranade, S. H. Bong, J. G. Sanjayan, and K. H. Khayat, "Fiber Orientation Effects on Ultra-High Performance Concrete Formed by 3D Printing," *Cement and Concrete Research* 143 (2021): 106384, https://doi.org/10.1016/j.cemconres.2021.106384.

44. E. Dong, Z. Jia, S. Rao, et al., "Fiber Alignment Mechanism in 3D-Printed Ultra-High Performance Concrete Based on Fluid Dynamics Theory," *Cement and Concrete Research* 198 (2025): 108011, https://doi.org/10.1016/j.cemconres.2025.108011.

45. Y. Wang, "Purdue University Graduate School. Thesis," (2024), https://doi.org/10.25394/PGS.27955488.V1.

46. N. Xu, Y. Qian, J. Yu, and C. K. Y. Leung, "Tensile Performance of 3D-Printed Strain-Hardening Cementitious Composites (SHCC) Considering Material Parameters, Nozzle Size and Printing Pattern," *Cement and Concrete Composites* 132 (2022): 104601, https://doi.org/10.1016/j.cemconcomp.2022.104601.

47. R. P. Behera and H. L. Ferrand, "Impact-Resistant Materials Inspired by the *Mantis shrimp's* Dactyl Club," *Matter* 4 (2021): 2831–2849.

48. S. Surehali, A. Tripathi, A. S. Nimbalkar, and N. Neithalath, "Anisotropic Chloride Transport in 3D Printed Concrete and Its Dependence on Layer Height and Interface Types," *Additive Manufacturing* 62 (2023): 103405.

49. F. B. Rodriguez, C. G. Lopez, Y. Wang, et al., "Evaluation of Durability of 3D-Printed Cementitious Materials for Potential Applications in Structures Exposed to Marine Environments," *RILEM Bookseries* 37 (2022): 175–181.

50. C. J. Adams, B. Bose, E. Mann, et al., "Superabsorbent Polymers for Internally Cured Concrete," *JTRP Technical Reports* (2021), https://doi.org/10.5703/1288284317366.

51. R. Bai, M. Lopez-Arias, and M. Velay-Lizancos, "Solar Reflectance Spectrum Modifications Produced by Metakaolin In Cement Paste: An Effective Alternative To Slag," *Construction and Building Materials* 504 (2025): 144639, https://doi.org/10.1016/j.conbuildmat.2025.144639.

52. G. Tanapornraweekit, P. Jiramarootapong, S. Paudel, S. Tangtermsirikul, and C. Snguanyat, "Experimental and Numerical Investigation of 3D-Printed Mortar Walls Under Uniform Axial Compression," *Construction and Building Materials* 360 (2022): 129552, https://doi.org/10.1016/j.conbuildmat.2022.129552.

53. Y. Wang, K. Bharadwaj, H. S. Esmaeeli, P. D. Zavattieri, O. B. Isgor, and W. J. Weiss, "Predicting Fracture from Thermodynamic Modeling of Cementitious Systems," *ACI Materials Journal* 120 (2023): 105.

54. A. Garnica, N. Suksangpanya, N. Yaraghi, et al., "Twisting Cracks in Bouligand Architectures Under Biaxial Conditions," *International Journal of Solids and Structures* 339 (2026): 114155, https://doi.org/10.1016/j.ijsolstr.2026.114155.

Supporting Information

Additional supporting information can be found online in the Supporting Information section.

Supporting File 1: adma75205-sup-0001-SuppMat.docx.